

# H I ABSORPTION SPECTRA TOWARD MAGPIS SUPERNOVA REMNANT CANDIDATES

A. K. JOHANSON AND C. R. KERTON

Department of Physics and Astronomy, Iowa State University, Ames, IA 50011, USA; [akj18@iastate.edu](mailto:akj18@iastate.edu), [kerton@iastate.edu](mailto:kerton@iastate.edu)

Received 2009 June 23; accepted 2009 September 23; published 2009 October 29

## ABSTRACT

The Multi-Array Galactic Plane Imaging Survey is an ongoing project to map out the northern Galactic plane in the 21 cm radio continuum. The survey identified 30 probable supernova remnant candidates in the Galactic plane from  $18^\circ < l < 32^\circ$ . H I absorption spectra were taken toward these sources using data from the VLA Galactic Plane Survey. Using both circular and hydrodynamical Galactic rotation models, the corresponding distances were calculated. Of the 30 candidates, distances to nine of them were determined, and another eight sources had their distances constrained with upper and lower bounds. Many of these sources have detectable radio recombination line emission toward them, and we comment on the possible nature of these emissions.

**Key words:** Galaxy: kinematics and dynamics – H II regions – supernova remnants – surveys

## 1. INTRODUCTION

H I absorption spectra combined with Galactic rotation models are a fundamental means of obtaining distances to supernova remnants (SNRs). For example, most of the SNR distances given in the Green (2009) SNR catalog were determined by H I absorption studies. In this paper, we combine spectral data from the VLA Galactic Plane Survey (VGPS; Stil et al. 2006) with both circular and new hydrodynamical Galactic rotation models of the inner Galaxy to find or constrain distances to 30 new SNR candidates identified by the Multi-Array Galactic Plane Imaging Survey (MAGPIS; Helfand et al. 2006), and found within the VGPS region.

In Section 2, we provide an overview of the VGPS and MAGPIS surveys. The H I absorption spectrum analysis technique is described in Section 3. In Section 4, we present our results including a discussion of notable and peculiar sources. Finally, we present our conclusions in Section 5.

## 2. OBSERVATIONS

MAGPIS is an ongoing 6'' resolution 21 cm radio continuum survey of the northern Galactic plane from  $5^\circ < l < 65^\circ$  and  $|b| \leq 1^\circ$  using the VLA in the B, C, and D configurations. Helfand et al. (2006) presented a list of 49 high-probability SNR candidates within  $5^\circ < l < 32^\circ$ . Candidates were identified based on the following criteria applied to the VLA and *Midcourse Space Experiment* (MSX; Price et al. 2001) data. First, the object has a high 20 cm (radio, VLA) to 21  $\mu$ m (infrared, MSX Band E) flux ratio. This distinguishes the nonthermal emission from SNRs from the thermal emission from H II regions. Second, since SNR spectra typically rise with decreasing frequency, the object should be detected in the available VLA 90 cm data with similar morphology and peak emission. Finally, objects need to have a shell morphology, which is typical for SNRs.

The SNR candidates from the MAGPIS survey were analyzed using data from the VGPS. The VGPS is a 1' resolution survey of 1420 MHz continuum emission and 21 cm H I line emission from  $18^\circ < l < 67^\circ$  and  $|b| \leq 1.3^\circ$ . The H I spectra have a velocity resolution of 1.56 km s<sup>−1</sup> and a channel spacing of 0.824 km s<sup>−1</sup>. Short-spacing line and continuum data were provided by the 100 m Green Bank Telescope (GBT), and the Effelsberg 100 m telescope, respectively. There are 30 MAGPIS

SNR candidates that fall in the overlapping  $18^\circ < l < 32^\circ$  region.

## 3. ANALYSIS

### 3.1. Determining the H I Opacity Spectrum

We followed the radiative transfer modeling and spectrum extraction technique of Tian et al. (2007). The H I brightness temperature on a line of sight toward a continuum source with a brightness temperature  $T_c$  in a continuum-subtracted data cube is

$$T_{B,\text{on}}(\nu) = T_s(\nu)(1 - e^{-\tau_\nu}) + T_c e^{-\tau_\nu} - T_c, \quad (1)$$

where  $T_s(\nu)$  is the spin temperature of the H I,  $\tau$  is the optical depth, and  $\nu$  is the Doppler shifted frequency of the 21 cm line, which we converted into a velocity. We designated the spectrum toward the source as the “ON” spectrum. The “OFF” source spectrum, taken along lines of sight close to the source, is given by

$$T_{B,\text{off}}(\nu) = T_s(\nu)(1 - e^{-\tau_\nu}) + T_{\text{bg}} e^{-\tau_\nu} - T_{\text{bg}}, \quad (2)$$

where  $T_{\text{bg}}$  represents background continuum emission. The opacity spectrum is obtained from a scaled difference of the ON and OFF spectra

$$e^{-\tau_\nu} - 1 = \frac{T_{B,\text{on}}(\nu) - T_{B,\text{off}}(\nu)}{\langle T_c \rangle - \langle T_{\text{bg}} \rangle}, \quad (3)$$

where  $\langle T_c \rangle$  and  $\langle T_{\text{bg}} \rangle$  are the average continuum brightness temperatures in the ON and OFF region, respectively. We note that in the case where  $\langle T_c \rangle \gg \langle T_{\text{bg}} \rangle$ , Equation (3) reduces to the standard formula (e.g., Normandeau 1999).

For each source, we have an H I data cube and a corresponding continuum image from the VGPS. We used the DRAO Export Software Package (Higgs et al. 1997) procedure MEANLEV to obtain the ON and OFF spectra. To use MEANLEV, the user defines a rectangular region around the source, two contour levels on the continuum map used to delineate the ON and OFF regions, and the background level in the OFF region. MEANLEV then averages the points within the ON region, weighted proportional to the square of the corresponding  $T_c$ , to define the ON spectrum, while the points outside the contour are averaged to define the OFF spectrum. MEANLEV then outputs the ON, OFF, and opacity spectrum for each source.

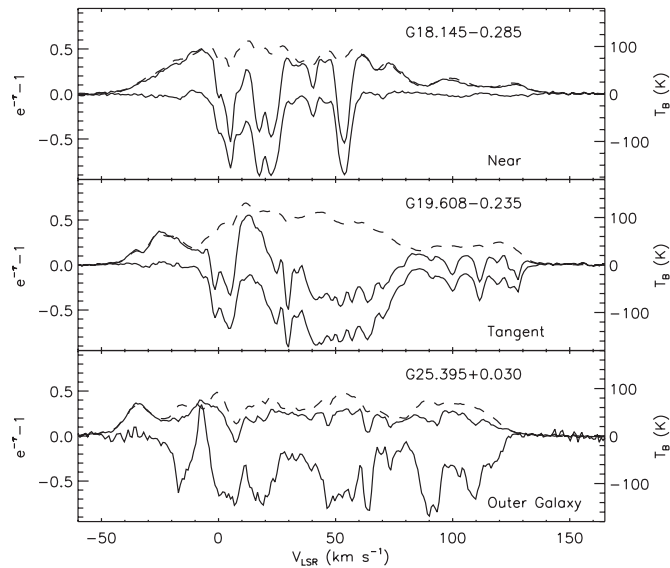


**Figure 1.** Near, tangent, and outer Galaxy scenarios. These bright Galactic sources illustrate the three basic types of opacity spectra seen toward the inner Galaxy. For each source, we show the ON and OFF emission spectra (upper solid line and dashed line, respectively, right axis) and the opacity spectrum (lower solid line, left axis). The upper panel shows an object at the near kinematic distance. The middle panel shows an object at a distance between the tangent point and the far solar circle distance. The lower panel shows an object beyond the solar circle in the outer Galaxy.

Three types of opacity spectra are possible for sources in the inner Galaxy. First, the absorption could extend all the way out to negative velocities. This would either place the object in the outer Galaxy, or indicate that it was an extragalactic source. The extragalactic case is unlikely because all of the MAGPIS SNR candidates were resolved at  $1'$ . Another possibility is to see absorption out to the tangent velocity, where the radial velocity along a particular line of sight reaches a maximum. The third possibility is to see absorption cease before the tangent velocity. An example of each case is presented in Figure 1. Each of these cases can be translated into distance determinations or constraints based on various Galactic rotation models (see Section 3.3).

### 3.2. Opacity Spectrum Analysis

Although obtaining an H I opacity spectrum is conceptually simple, in order to obtain useful results care must be taken in identifying the noise level in the spectrum, especially for extended low surface brightness objects where the opacity signal can be low. There are a number of effects that can result in noise in the opacity spectrum which mimic the continuum absorption signal. First, there is instrumental noise in the H I spectra. This can be quantified by calculating the standard deviation of the opacity spectrum in the spectrometer end channels which correspond to velocities where there is no H I. We denote this error estimate as  $\sigma_{\text{base}}$ . Second, there is a more dominant uncertainty related to our estimate of the OFF spectrum. Because MEANLEV averages over all the pixels outside a designated contour, small-scale variations across the region in the H I brightness temperature lead to errors in the spectrum. We define the standard deviation of the brightness temperature of the pixels used in the OFF spectrum, as  $\sigma_{\text{off}}$ . Finally, large-scale (arcminute or larger) coherent variations in the H I brightness temperature structure (e.g., filaments) can mimic an absorption signal (see Figure 2). To quantify this noise signal due to H I

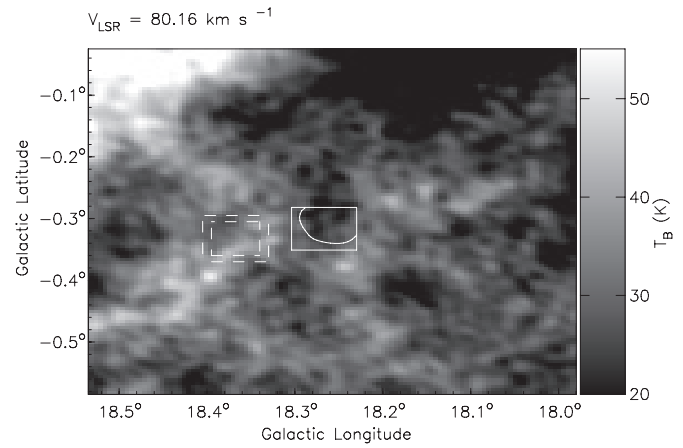


**Figure 2.** False absorption signal. The image shows a velocity channel from a VGPS H I data cube. The central rectangle shows the region of interest for source G18.25-0.31, and the contour indicates the ON and OFF boundary within the region. The large-scale H I structure is such that the ON spectrum is lower than the OFF spectrum producing a false absorption signal. Because there is little small-scale variation in the OFF region, the  $\sigma_{\text{off}}$  error estimate does not catch this. The  $\sigma_{\text{H}}$  estimate was developed to quantify the uncertainty caused by these larger-scale variations in H I brightness temperature (see Section 3.2 for details). The dashed-line boxes to the left show the region used in determining  $\sigma_{\text{H}}$ . The inner box is the false ON region and the outer shows the limits of the OFF.

structure, we define a region away from any continuum sources and perform the same sort of analysis, producing an OFF-OFF spectrum. We define the standard deviation from the average of this spectrum as  $\sigma_{\text{H}}$ . Our final error estimate is defined as  $\sigma_{\text{tot}} = \max[3\sigma_{\text{base}}, \sigma_{\text{off}}, 3\sigma_{\text{H}}]$ . We ignored absorption-like features with opacity less than  $\sigma_{\text{tot}}$  in our velocity analysis.

### 3.3. Distance Determination from the Galactic Rotation Models

A model for the motion of gas in the Galaxy can be used to derive a velocity-distance curve which shows the radial velocity of the gas as a function of the distance from the Sun. For this study, we used two models: one based on a smooth model fit to tangent point velocities inside the solar radius ( $R_o = 8.5$  kpc), with a flat rotation curve ( $V_o = 220$  km s $^{-1}$ ) beyond the Sun, and another based on the hydrodynamical models of Pohl et al. (2008) with  $R_o = 7.5$  kpc. To illustrate the typical form of the velocity-distance curves in this part of the Galaxy, Figure 3 shows the curves for  $l = 25^\circ$ . The main offset between the two curves is due to the different values of  $R_o$ . The Pohl et al. (2008) model curves typically have a broader peak around the tangent point velocity and the “wiggles” in the curve, associated with non-circular motions in the inner Galaxy, result in multiple “near” and “far” kinematic distances for certain velocities. Both models use flat rotation curves beyond the solar circle so the shapes of the curves for negative velocities are the same.

For each opacity spectrum, we can obtain a distance or distance constraint from the models as follows. For objects with absorption out to negative velocities, there is only one corresponding distance beyond the solar circle. For objects with absorption ending closer than the tangent point, we know the object is at the near kinematic distance. For objects with absorption to the tangent point, it is impossible to assign a unique velocity to that object. The object must be at a minimum distance of that corresponding to the tangent point velocity and at a maximum distance corresponding to where the line of sight intersects the solar circle. This gives an upper and lower bound for the distance.

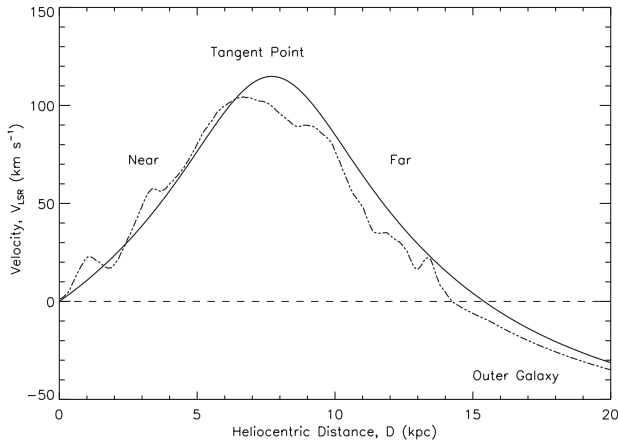


**Figure 3.** Velocity–distance curves for  $l = 25^\circ$ . The solid line is for a smooth inner Galaxy model plus flat rotation curve, and the dot-dashed line is for the hydrodynamical models of Pohl et al. (2008). The offset in distance between the two models is primarily due to the use of different  $R_0$  values. The wiggles in the Pohl et al. (2008) curve are caused by non-circular motions associated with spiral arm and bar structures in the inner Galaxy.

**Table 1**  
Distances to SNR Candidates

| Name<br>(Gl+b)               | $V_{\text{LSR}}$<br>(km s $^{-1}$ ) | $D_{\text{circ}}$<br>(kpc) | $D_{\text{Pohl}}$<br>(kpc) | $V_{\text{RRL}}^a$<br>(km s $^{-1}$ ) | Comments          |
|------------------------------|-------------------------------------|----------------------------|----------------------------|---------------------------------------|-------------------|
| G18.1500–0.1722 <sup>b</sup> | 102                                 | $6.3 \pm 0.5$              | $6.2 \pm 0.1$              | ...                                   | ...               |
| G18.2536–0.3083              | 42                                  | $4.3 \pm 0.6$              | $3.3 \pm 0.5$              | 50.9                                  | H II <sup>c</sup> |
| G18.6375–0.2917 <sup>b</sup> | 62                                  | $4.6 \pm 0.6$              | $4.9 \pm 0.3$              | 71.1                                  | ...               |
| G18.7583–0.0736              | 68                                  | $4.9 \pm 0.5$              | $5.3 \pm 0.1$              | ...                                   | ...               |
| G19.5800–0.2400              | 103                                 | $6.3 \pm 0.5$              | $6.5 \pm 0.1$              | 41.0                                  | H II <sup>d</sup> |
| G19.6100–0.1200              | 125                                 | $11.6 \pm 0.5$             | $11.1 \pm 0.3$             | 58.6                                  | H II              |
| G22.7583–0.4917              | 78                                  | $5.1 \pm 0.6$              | $4.9 \pm 0.2$              | 74.8                                  | H II <sup>c</sup> |
| G22.9917–0.3583              | 75                                  | $5.0 \pm 0.5$              | $4.8 \pm 0.1$              | 74.1                                  | H II              |
| G23.5667–0.0333              | 102                                 | $6.4 \pm 0.7$              | $6.0 \pm 0.2$              | 91.3                                  | d                 |

**Notes.**

<sup>a</sup> Velocities obtained from Lockman (1989).

<sup>b</sup> Brogan et al. (2006) SNR.

<sup>c</sup> H II indicates the object is actually an H II region.

<sup>d</sup> SNR candidate was separated from line of sight H II regions.

<sup>e</sup> SNR candidate could not be separated from line of sight H II regions.

#### 4. RESULTS

Out of the 30 SNR candidates, eight had opacity spectra terminating at velocities before the tangent point and nine had absorption out to the tangent point. Their spectra are plotted in Figures 4 and 5. The opacity spectra of the remaining candidates had too weak a signal compared to noise levels for a distance determination to be made. Distances for nine of the spectra were determined, eight with opacity spectra corresponding to near kinematic distances and one tangent point opacity spectrum where a separate determination of the velocity was available allowing us to place the source at the far kinematic distance (see Section 4.2). These distances are listed in Table 1 and were calculated based on the models described in Section 3.3. The error estimates for these distances assume the bulk motions of the H I, apart from their orbital motions, are on the order of 10 km s $^{-1}$  (e.g., Fish et al. 2003). We therefore also considered the possibility that objects with absorption within 10 km s $^{-1}$  of the tangent velocity could be at the tangent point, and constrained the distances in those cases with the lower bound corresponding to the near kinematic distance and the upper bound corresponding to the far solar circle. The constraints on the distances to objects with tangent point opacity spectra are

**Table 2**  
Constraints on Distances to SNR Candidates

| Name<br>(Gl+b)  | $D_{\text{circ}}$<br>(kpc) | $D_{\text{Pohl}}$<br>(kpc) | $V_{\text{RRL}}^a$<br>(km s $^{-1}$ ) | Comments |
|-----------------|----------------------------|----------------------------|---------------------------------------|----------|
| G19.4611+0.1444 | 6.8–17.5                   | 6.3–16.5                   | 19.8                                  | b        |
| G27.1333+0.0333 | 6.1–16.2                   | 5.5–15.2                   | 90.2                                  | c        |
| G28.5167+0.1333 | 6.2–15.9                   | 5.5–14.9                   | ...                                   | ...      |
| G28.5583–0.0083 | 6.5–15.9                   | 5.5–15.0                   | ...                                   | ...      |
| G29.3667+0.1000 | 5.8–15.8                   | 5.2–14.9                   | ...                                   | ...      |
| G30.8486+0.1333 | 6.7–15.6                   | 5.2–14.6                   | 100                                   | b        |
| G31.0583+0.4833 | 6.6–15.5                   | 5.2–14.6                   | 27.9                                  | d        |
| G31.6097+0.3347 | 6.6–15.4                   | 5.2–14.6                   | ...                                   | ...      |

**Notes.**

<sup>a</sup> Velocities obtained from Lockman (1989).

<sup>b</sup> SNR candidate was separated from line-of-sight H II regions.

<sup>c</sup> No infrared emission is associated with this source.

<sup>d</sup> SNR candidate could not be separated from line-of-sight H II regions.

**Table 3**  
SNR Candidates with Unknown Distances

| Name<br>(Gl+b)               | Peak $T_{B,1420}$<br>(K) | Comments          |
|------------------------------|--------------------------|-------------------|
| G19.5917+0.0250              | 29                       | ...               |
| G19.6600–0.2200              | 42                       | H II <sup>a</sup> |
| G20.4667+0.1500 <sup>b</sup> | 35                       | ...               |
| G21.5569–0.1028              | 24                       | ...               |
| G21.6417+0.0000              | 29                       | ...               |
| G22.3833+0.1000              | 34                       | ...               |
| G24.1803+0.2167              | 37                       | H II              |
| G25.2222+0.2917              | 38                       | ...               |
| G28.3750+0.2028              | 31                       | ...               |
| G28.7667–0.4250              | 26                       | ...               |
| G29.0667–0.6750              | 28                       | H II              |
| G29.0778+0.4542              | 41                       | ...               |
| G31.8208–0.1222              | 37                       | ...               |

**Notes.**

<sup>a</sup> H II indicates the object is actually an H II region.

<sup>b</sup> Brogan et al. (2006) SNR.

listed in Table 2. For completeness, Table 3 lists the names and peak VGPS continuum brightness temperatures of the sources which were not bright enough to allow us to obtain reliable opacity spectra.

##### 4.1. Revisiting the SNR Candidate List

Surprisingly, we found that 16 of the 30 MAGPIS SNR candidates have detectable radio recombination line (RRL) emission reported in the Lockman (1989) survey (L89 hereafter) done with the NRAO 43 m (140 foot) telescope (3' beam). Strong RRL emission from SNRs is not expected (Downes & Wilson 1974; Foster et al. 2006) and the association with the SNR candidates is likely due to either emission from unrelated H II regions close to the SNR or the misclassification of the SNR candidate. The first case is possible given the inner Galaxy location of the candidate and the beam size difference between the RRL survey and MAGPIS. Misclassification is most likely related to the relatively poor sensitivity of the MSX Band E data which may result in missing associated infrared emission. We reinvestigated these sources using higher resolution and sensitivity data from the *Spitzer* GLIMPSE (Benjamin et al. 2003) and MIPS GAL (Carey et al. 2009) surveys.<sup>1</sup> Our findings

<sup>1</sup> False-color images of the various *Spitzer* and MAGPIS data sets can easily be created using the MAGPIS Web site, <http://third.ucllnl.org/gps/index.html>.

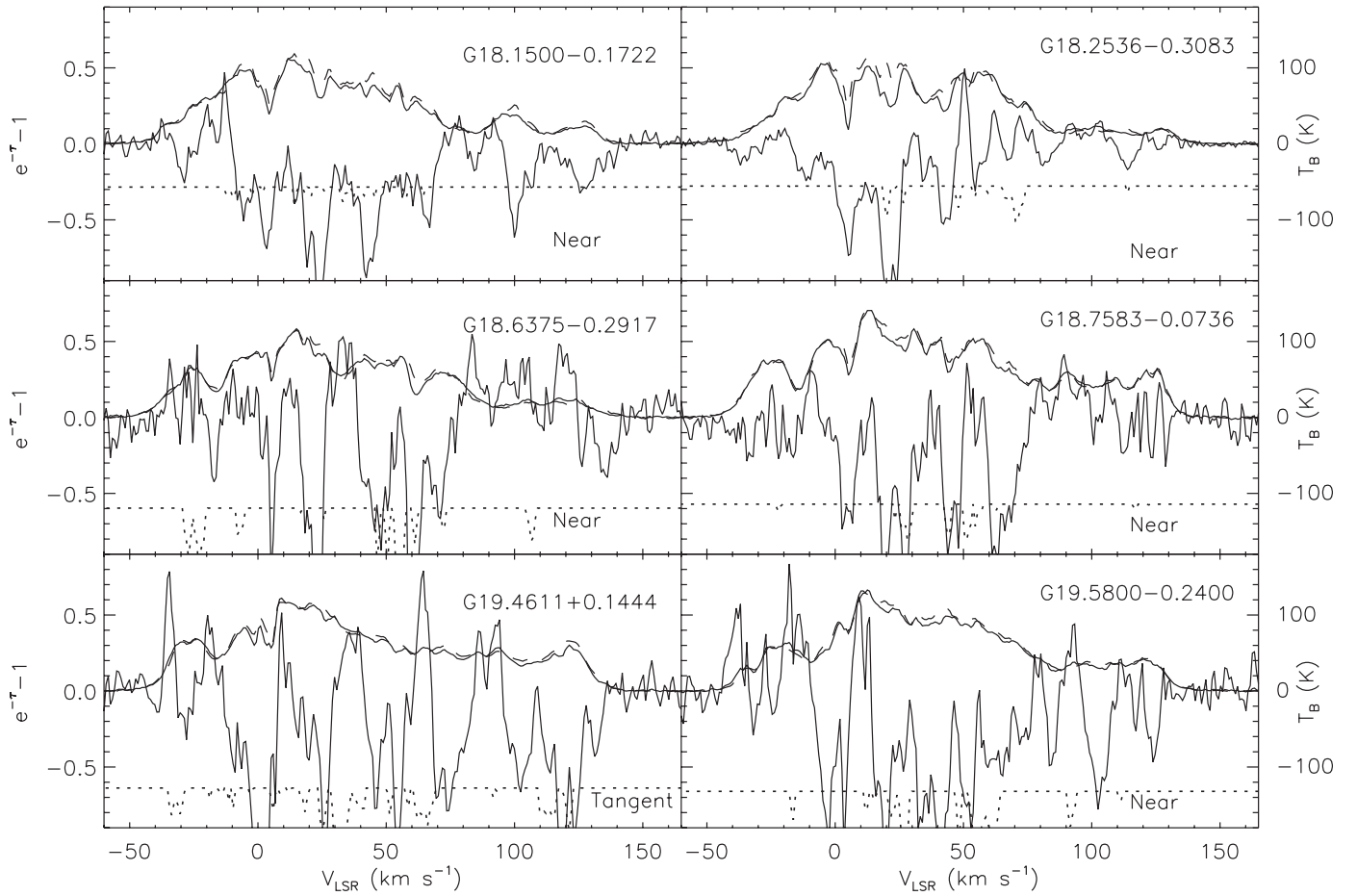


**Figure 4.** H I emission and opacity spectra toward MAGPIS SNR candidates from  $18^\circ < l < 19^\circ 6$ . For each source, we show the ON and OFF emission spectra (upper solid line and dashed line, respectively, right axis) and the opacity spectrum with its error estimate (lower solid line and dotted line, respectively, left axis). Only sources where a distance or constraint could be obtained are shown. The name of the source, as well as whether it is classified as near or tangent is also indicated.

are discussed in the next section, and we indicate in Tables 1 and 2 the value of any associated RRL emission and specify which candidates are actually H II regions.

#### 4.2. Notable Sources

*G18.25-0.31.* This object has a  $3'$  shell structure in the MAGPIS 20 cm radio image. L89 reported an RRL detection toward a part of the shell which corresponds to an extremely bright arc of mid-infrared emission visible in the *MSX*  $21\ \mu\text{m}$  image and is saturated in the MIPS GAL  $24\ \mu\text{m}$  image. In the GLIMPSE  $8\ \mu\text{m}$  images, we see that the shell of radio emission is surrounded by polycyclic aromatic hydrocarbon (PAH) emission, a structure typically seen for H II regions. We conclude that G18.25-0.31 is an H II region and suggest that the bright mid-infrared arc could be an associated massive young stellar object.

*G18.64-0.29.* This object shows a  $4'$  arc in the MAGPIS 20 cm radio image. The *MSX*  $21\ \mu\text{m}$  shows no detectable analog. The GLIMPSE  $8\ \mu\text{m}$  shows faint diffuse emission throughout the surrounding region. The MIPS GAL  $24\ \mu\text{m}$  band, however, clearly shows a structure analogous to the radio arc. A spectral index study done by Brogan et al. (2006) identified this object as an SNR, but L89 was able to obtain RRL measurements toward this source and they identified it as an H II region. It is possible

that the RRL detection is associated with the nearby large W39 H II region.

*G19.46+0.14.* The MAGPIS radio image shows a diffuse  $4'$  shell with two brighter compact sources in the line of sight. The brighter of the two compact regions is visible in the *MSX*  $21\ \mu\text{m}$  image. GLIMPSE  $8\ \mu\text{m}$  and MIPS GAL  $24\ \mu\text{m}$  show a PAH shell and dust emission associated with both compact sources, indicating they are H II regions. The RRL detection reported by L89 is no doubt associated with these H II regions. The two compact sources were masked out of the data when the opacity spectrum was taken. The diffuse shell is surrounded on the lower part by  $8\ \mu\text{m}$  emission, but not in the upper portion. Since it lacks a full ring of PAH emission and lacks  $24\ \mu\text{m}$  emission, we conclude the diffuse shell is probably a SNR.

*G19.58-0.24 and G19.66-0.22.* A very bright H II region sits in the center of these two SNR candidates. The MAGPIS radio image shows two shell structures on opposite edges of the H II region. The *MSX*  $21\ \mu\text{m}$  image shows emission along the edges close to the central H II region, following the boundaries of the SNR candidates. However, there is no other  $21\ \mu\text{m}$  emission along the outer edges or in the shells. The MIPS GAL  $24\ \mu\text{m}$  image supports the *MSX* data. The GLIMPSE data show something similar, with PAH emission following the edges of the shells closest to the H II region and fading toward the outer regions. RRL emission was detected by L89 toward this region.



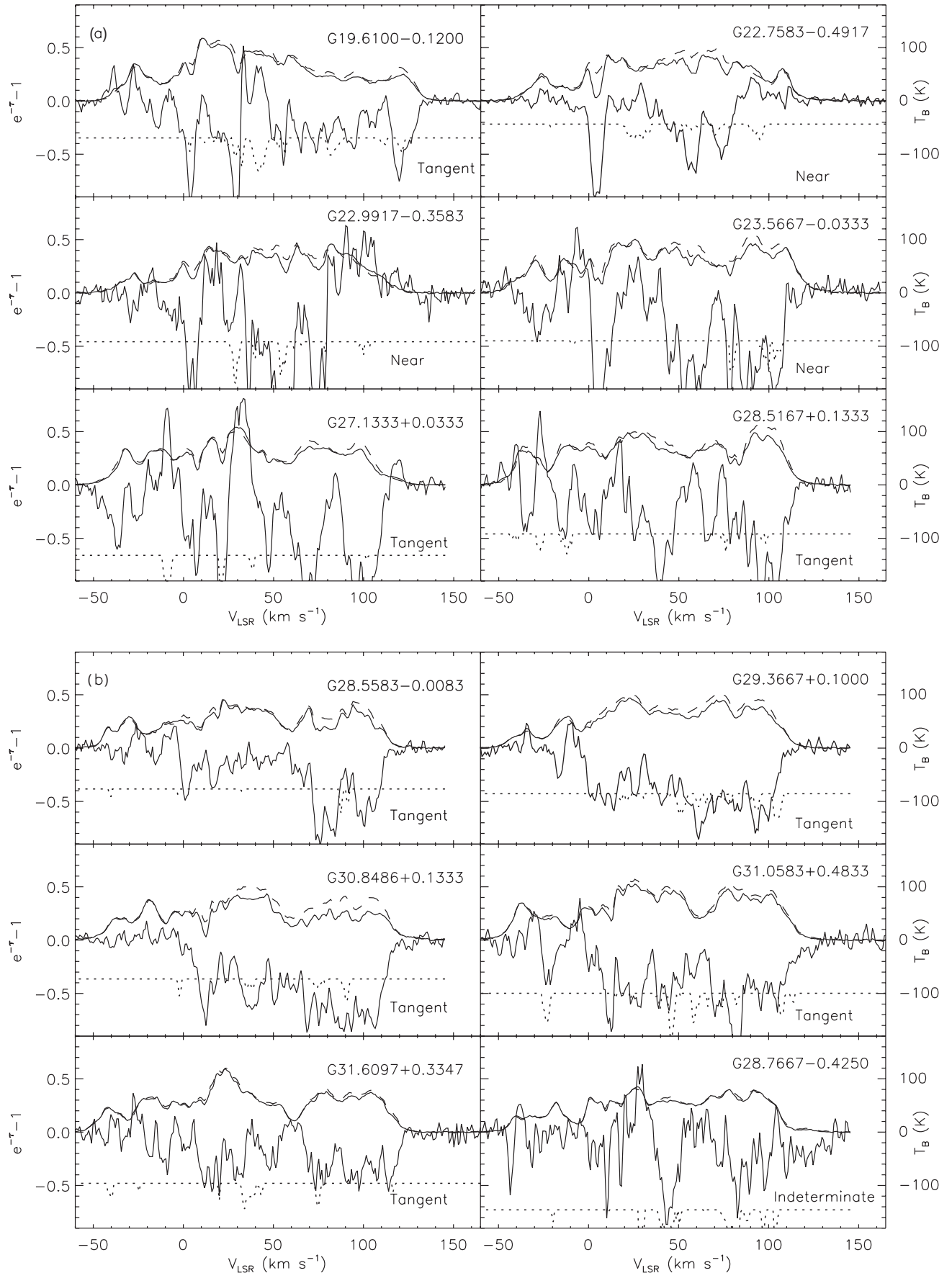


**Figure 5.** Same as Figure 4 for MAGPIS SNR candidates from  $19^{\circ}6' < l < 32^{\circ}$ . The spectra toward G28.7667-0.4250 is shown as an example of a source where we were unable to determine a distance.

An opacity spectrum toward the H II region shows absorption out to the tangent velocity, indicating it is located at the far kinematic distance. The bright H II region was masked out of the data when the opacity spectra for the two SNR candidates were obtained. The opacity spectrum toward G19.58–0.24 indicates it is located at the near kinematic distance. The signal-to-noise ratio toward G19.66–0.22 was too low to obtain a reliable opacity spectrum. We conclude that the H II region is simply a background object not associated with the SNR candidates, which we also believe are H II regions because of associated infrared emission at both 8 and 24  $\mu\text{m}$ .

*G19.61–0.12.* The MAGPIS radio data show a relatively compact bright region and a prominent northern arc. These two primary features are not distinguishable at the resolution of the VGPS. The *MSX* and MIPS GAL data show bright diffuse emission throughout the region, except for the northern arc. The GLIMPSE 8  $\mu\text{m}$  image, however, shows associated emission lining the edges of the entire region, including the northern arc. L89 reported an RRL detection toward this region. This is an H II region with absorption out to the tangent point, placing it at the far kinematic distance corresponding to L89's measurement (see Table 1).

*G20.47+0.15.* This source looks like an 8' shell in the MAGPIS radio image. The *MSX* 21  $\mu\text{m}$  data show no associated emission, but the corresponding 24  $\mu\text{m}$  MIPS GAL data show emission with the same structure as the radio data. The 8  $\mu\text{m}$  emission is faint and shows no shell surrounding the region. The source was too faint for us to obtain a reliable spectrum. L89 was able to detect RRL emission, but Brogan et al. (2006) identified this source as an SNR from the spectral index study. The lack of a PAH shell leads us to conclude that the source is a SNR.

*G22.38+0.10.* The radio data from MAGPIS show a faint arc structure near a bright, compact source. The *MSX* 21  $\mu\text{m}$  infrared data show emission from the compact source, indicating an H II region. The more sensitive MIPS GAL infrared data show a complex system of H II regions with two prominent arcs, one of which is oriented along the radio arc, but is much smaller in size. L89 obtained an RRL detection and may have picked up the smaller arc in the line of sight of the radio arc. The GLIMPSE data show PAH emission associated with the complex system including the two infrared arcs but not the larger radio arc. We conclude the larger radio arc is an SNR, but the complexity of the system prevented us from obtaining a reliable spectrum.

*G22.76–0.49.* The MAGPIS radio image shows a bright compact region and two different arc structures. Strong infrared emission in *MSX* and MIPS GAL images shows that the compact source is an H II region. The arcs are not visible in the *MSX* or MIPS GAL data, but the GLIMPSE data show 8  $\mu\text{m}$  emission throughout the entire region, following the arc edges, leading us to conclude that they are part of another H II region. We do not believe that the arcs are associated with the compact H II region because they are invisible in the 24  $\mu\text{m}$  image. Unfortunately, these arc structures could not be separated from the compact H II region at the VGPS resolution. The velocity obtained from the opacity spectrum matched the L89 RRL measurements toward the system.

*G22.99–0.36.* The MAGPIS radio image of this source shows a 3' shell. This shell is not visible in the *MSX* 21  $\mu\text{m}$  image. The shell is clearly visible in the MIPS GAL data, however, and the GLIMPSE data show the PAH emission perfectly outlining the shell. L89 obtained an RRL velocity matching our results. This object is an H II region.

*G23.57–0.03.* The MAGPIS radio image shows a faint, large 8' diameter shell, with a brighter compact region in the line of sight. The *MSX* 21  $\mu\text{m}$  data show that the compact region is an H II region in the line of sight toward the SNR candidate. L89 also measured an RRL velocity toward the object. This area was masked out of the data when the opacity spectrum was obtained. The MIPS GAL and GLIMPSE data show no corresponding emission with the large shell, so we conclude it is an SNR.

*G24.18+0.22.* The MAGPIS radio image shows a 5' shell with slightly brighter emission from a more compact region near the bottom. The *MSX* 21  $\mu\text{m}$  data show no associated infrared emission with this region. The MIPS GAL data show that the compact source has associated 24  $\mu\text{m}$  emission, but not the shell as a whole. L89 obtained an RRL measurement toward the lower compact region. The GLIMPSE image shows 8  $\mu\text{m}$  emission surrounding the larger shell. The signal-to-noise ratio was too low to obtain a reliable opacity spectrum. Both the compact region and larger shell are probably H II regions.

*G27.13+0.03.* The MAGPIS radio image shows a prominent 10' arc. There is no corresponding infrared emission at any wavelength from any of the other surveys, which makes the L89 RRL detection very curious. The absorption in the opacity spectrum went out to the tangent point, so we do not have another measurement of the source's velocity to compare with the RRL data. There is a relatively faint compact H II region 3' away from L89's telescope pointing, which may account for the RRL detection. There is no doubt though that G27.13+0.03 is an SNR.

*G29.07–0.68.* The 20 cm MAGPIS radio image shows a 10' shell. The *MSX* 21  $\mu\text{m}$  data show no associated infrared emission with this region. The MIPS GAL data show that the center is filled with 24  $\mu\text{m}$  emission and the GLIMPSE data show that the entire region is surrounded by PAH emission. L89 obtained an RRL velocity toward this source, which is clearly an H II region. We were unable to obtain a useful opacity spectrum toward this source.

*G30.85+0.13.* There is a 2' shell in the MAGPIS radio image only 30'' away from a bright, compact source. The bright compact source has associated *MSX* 21  $\mu\text{m}$  emission, and the higher resolution MAGPIS data and GLIMPSE data also show emission from the compact source identifying it as an H II region. L89 reported an RRL detection toward this region, but we are confident it came from the compact H II region. The H II region was masked out of the data when the opacity spectrum was obtained. There is no associated infrared emission with the shell and it is correctly identified as an SNR.

*G31.06+0.48.* The MAGPIS radio image of this region shows a complex structure of arcs and compact sources. There is one prominent arc that is distinct from the rest of the complex. The *MSX* 21  $\mu\text{m}$  data show faint emission from the central region, and the prominent arc is not visible. The MIPS GAL data show several bright, compact H II regions in the complex, much more than is visible in the *MSX* data. There is no corresponding emission from the arc structure in the MIPS GAL or the GLIMPSE data. The GLIMPSE data do show emission throughout the complex region. The arc and the central region could not be separated in the VGPS data. L89 measured RRL emission from the central complex, and absorption to the tangent point places the complex at the far kinematic distance. The prominent arc is probably an SNR.

## 5. CONCLUSIONS

Using data from the VGPS, absorption and emission spectra were taken toward MAGPIS SNR candidates. The radial

velocities and corresponding distances to nine of these sources were determined from the resulting opacity spectra. For eight sources only lower and upper limits on their distance could be determined. We reexamined all of the SNR candidates with RRL detections reported in L89 and determined that eight of the sources were not SNRs, but rather H II regions. Since L89 had a separate velocity determination for these objects, the far and near kinematic distance ambiguity could be resolved with the opacity spectra. The primary reason for misidentification was the low sensitivity of the *MSX* Band E data used for infrared detection. The more sensitive MIPS GAL 24  $\mu\text{m}$  data and the GLIMPSE 8  $\mu\text{m}$  data, tracing the PAH emission, proved to be very useful in identifying H II regions.

It is clear that the more sensitive GLIMPSE 8  $\mu\text{m}$  and MIPS GAL 24  $\mu\text{m}$  data will produce a better indication of thermal sources as MAGPIS continues its survey covering the rest of the northern Galactic plane. H I absorption spectra from the VGPS can be used to determine the distances to many of the candidates, but higher resolution H I data, matching the resolution of the MAGPIS continuum data, would be very useful for determining distances to new SNR found in complex regions where it is difficult to separate H II region and SNR emission.

This research used the facilities of the Canadian Astronomy Data Centre operated by the National Research Council of

Canada with the support of the Canadian Space Agency. This work is also based on observations made with the *Spitzer Space Telescope*, which is operated by the Jet Propulsion Laboratory (JPL), California Institute of Technology, under NASA.

## REFERENCES

- Benjamin, R. A., et al. 2003, *PASP*, **115**, 953  
 Brogan, C. L., Gelfand, J. D., Gaensler, B. M., Kassim, N. E., & Lazio, T. J. W. 2006, *ApJ*, **639**, L25  
 Carey, S. J., et al. 2009, *PASP*, **121**, 76  
 Downes, D., & Wilson, T. L. 1974, *A&A*, **34**, 133  
 Fish, V. L., Reid, M. J., & Wilner, D. J. 2003, *ApJ*, **587**, 701  
 Foster, T., Kothes, R., Sun, X. H., Reich, W., & Han, J. L. 2006, *A&A*, **454**, 517  
 Green, D. A. 2009, *Bull. Astron. Soc. India*, **37**, 45  
 Helfand, D. J., Becker, R. H., White, R. L., Fallon, A., & Tuttle, S. 2006, *AJ*, **131**, 2525  
 Higgs, L. A., Hoffmann, A. P., & Willis, A. G. 1997, in ASP Conf. Ser. 125, *Astronomical Data Analysis Software and Systems VI*, ed. G. Hunt & H. E. Payne (San Francisco, CA: ASP), 58  
 Lockman, F. J. 1989, *ApJS*, **71**, 469  
 Normandeau, M. 1999, *AJ*, **117**, 2440  
 Pohl, M., Englmaier, P., & Bissantz, N. 2008, *ApJ*, **677**, 283  
 Price, S. D., Egan, M. P., Carey, S. J., Mizuno, D. R., & Kuchar, T. A. 2001, *AJ*, **121**, 2819  
 Stil, J. M., et al. 2006, *AJ*, **132**, 1158  
 Tian, W. W., Leahy, D. A., & Wang, Q. D. 2007, *A&A*, **474**, 541